Soils and Foundations 2012;52(3):393–410

The Japanese Geotechnical Society

Soils and Foundations

www.sciencedirect.com
journal homepage: www.elsevier.com/locate/sandf

Behaviour of displacement piles in sand under cyclic axial loading

C.H.C. Tsuha[a,1], P.Y. Foray[b], R.J. Jardine[c], Z.X. Yang[d,*,2], M. Silva[b], S. Rimoy[c]

[a]University of São Paulo at São Carlos, Department of Geotechnical Engineering, Av. Trabalhador Sãocarlense, 400, São Carlos, SP 13566-590, Brazil
[b]Institut National Polytechnique de Grenoble, Laboratoire 3S-R (INP-UJF-CNRS), Domaine Universitaire BP53, Grenoble 38041, France
[c]Imperial College, Department of Civil and Environmental Engineering, London SW7 2AZ, UK
[d]Department of Civil Engineering, Zhejiang University, 866 Yuhangtang, Zijingang Campus, Hangzhou 310058, China

Available online 8 June 2012

Abstract

Field experiments have demonstrated that piles driven into sand can respond to axial cyclic loading in Stable, Unstable or Meta-Stable ways, depending on the combinations of mean and cyclic loads and the number of cycles. An understanding of the three styles of responses is provided by experiments involving a highly instrumented model displacement pile and an array of soil stress sensors installed in fine sand in a pressurised calibration chamber. The different patterns of effective stress developing on and around the shaft are reported, along with the results of static load tests that track the effects on shaft capacity. The interpretation links these observations to the sand's stress–strain behaviour. The interface-shear characteristics, the kinematic yielding, the local densification, the growth of a fractured interface-shear zone and the restrained dilatancy at the pile–soil interface are all found to be important. The model tests are shown to be compatible with the full-scale behaviour and to provide key information for improving the modelling and the design rules.
© 2012 The Japanese Geotechnical Society. Production and hosting by Elsevier B.V. All rights reserved.

Keywords: Displacement pile; Cyclic loading; Pile–soil interface; Dilatancy; Calibration chamber; Local stresses

1. Introduction

1.1. Earlier studies

The safe operation of installations, such as offshore structures, wind turbines, pylons or silos, relies on the ability of their foundations to sustain cyclic loading. Model tests by Chan and Hanna (1980) showed that the cyclic response of displacement piles in sand is affected by the number (N) and the frequency (f) of cycles, the mean shaft load (Q_{mean}) and the shaft cyclic amplitude (Q_{cyclic}), as defined in Fig. 1, the pile depth (L), the loading history and the sand characteristics. Distinctions are also often drawn between two-way (TW) loading, that involves both tension and compression loads, and one-way (OW) cycling, that involves loads of only one sign.

Jardine and Standing (2000) reported the results of cyclic tests on seven open-tube steel piles, 457 mm in diameter, driven above and below the water table in

*Corresponding author. Tel.: +86 571 8820 8476; fax: +86 571 8820 8475.
E-mail addresses: chctsuha@sc.usp.br (C.H.C. Tsuha), Pierre.Foray@grenoble-inp.fr (P.Y. Foray), r.jardine@imperial.ac.uk (R.J. Jardine), zxyang@zju.edu.cn (Z.X. Yang), matias.silva@hmg.inpg.fr (M. Silva), siya.rimoy@imperial.ac.uk (S. Rimoy).
[1]Formerly INPG Grenoble, France and Laboratoire 3S-R (INP-UJF-CNRS), France.
[2]Formerly Imperial College, London SW7 2AZ, UK.
Peer review under responsibility of The Japanese Geotechnical Society.

Production and hosting by Elsevier

0038-0806 © 2012 The Japanese Geotechnical Society. Production and hosting by Elsevier B.V. All rights reserved.
http://dx.doi.org/10.1016/j.sandf.2012.05.002

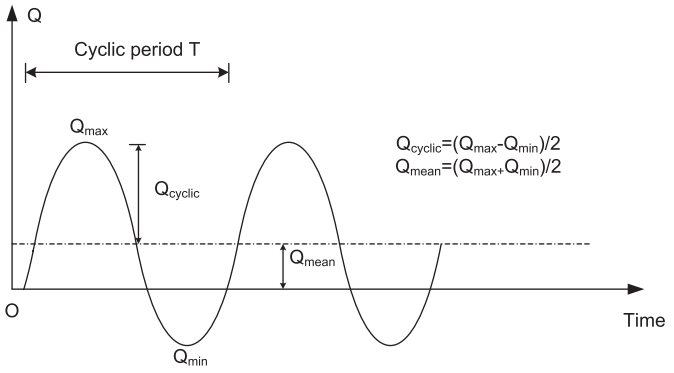


Fig. 1. Definition of cyclic loading parameters for both field and laboratory model tests. *Note*: The same system applies to local shear stressses τ_{rz} in Fig. 3.

clean medium-to-dense marine sand at Dunkerque, France.[3] Fig. 2 presents a summary interaction diagram describing the cyclic shaft failure conditions interpreted from load-controlled tests. The number of cycles, N_f, (applied in ≈ 60 s periods), required to reach failure, is related to Q_{mean} and Q_{cyclic}, normalised by the static shaft tension capacity, Q_T, available just before cycling. Rate effects and pore pressure generation were insignificant over the ranges considered, so the criterion that no tension cycle can apply a shaft load greater than Q_T applies. Three styles of responses are identified in Fig. 2:

- *A Stable (S) Zone*, where axial displacements stabilise or accumulate very slowly over hundreds of cycles, under either TW or OW (in this case, tensile) loading. It was noted that such cycles can improve shaft capacity.
- *An Unstable (US) Zone*, where displacements accumulate rapidly under OW or TW cycling. Shaft capacity falls markedly. For example, failure is expected after 100–200 TW cycles applied at the $Q_{cyclic}/Q_T=0.5$, $Q_{mean}/Q_T=0$ level, even though the equivalent static factor of safety is 2.
- *An intermediate Meta-Stable (MS) Zone*, where displacements accumulate at moderate rates over tens of cycles without stabilising. Cyclic failure develops with $100 < N < 1000$.

The pattern outlined in Fig. 2 is likely to vary with soil conditions and pile parameters. Limited suites of field cyclic tests were performed with Imperial College Instrumented (ICP) displacement piles, 102 mm in diameter, in clean sand of widely different relative densities (above and below the water tables) at Labenne and Dunkerque in France (Lehane, 1992; Lehane et al., 1993; Chow, 1997). They all showed zero excess pore water pressure generation during installation and static and (relatively slow) cyclic testing. The combinations of cyclic and average local shear stress τ_{rz} required to reach failure, which were measured directly on the pile surface, are presented in Fig. 3 (denoted as τ_{cyclic} and τ_{mean} following Fig. 1) and normalised by local shaft shear capacity (denoted as $\tau_{max\ static}$). The interpreted cyclic failure lines are broadly comparable to the full-scale trends shown in Fig. 2. These, and other experiments by Chow (1997) at Dunkerque on a larger instrumented steel open-pipe pile, confirmed the top-down process of progressive failure suggested by Jardine (1991, 1994).

The ICP experiments also identified critical new findings regarding the interface effective stress regimes of displacement piles, showing that the local radial effective stress and the limiting shaft shear stress, developing at any particular depth and depending directly on local CPT resistance q_c, are strongly affected by relative pile tip depth h (normalised by the pile radius R) and only weakly affected by local free-field vertical effective stress σ'_{vo}. The operational, critical state, interface shear angle δ is controlled by the sand's granulometry, as well as by the shaft material and the roughness; it is independent of the sand density. Straining at the pile–soil interface during loading is constrained kinematically. The rigid pile and its relatively rough surface prevent any vertical or circumferential straining close to the pile–soil interface. Any drained radial straining is constrained (in dry or saturated sand) by the shear stiffness of the surrounding soil, leading to an inverse radial scale effect. Neither volume change nor radial straining can take place in low-permeability saturated soil under short-duration undrained loading, although the local pore pressure and total stress may change. ICP tests on clay show that slowly drained and rapidly undrained loading tests engender closely comparable interface effective stress paths (Lehane, 1992; Chow, 1997).

The above key features are captured by the 'ICP' sand design procedures (Jardine et al., 2005) that, with other related 'CPT' procedures, are applied widely in designing large piles driven into relatively permeable (saturated or dry) silica sand under essentially drained conditions (API, 2008). Piles installed in clayey soil, that remains essentially undrained during installation, may be treated by the parallel ICP clay procedure. Piezocone profiling provides critical information regarding potential drainage conditions; simplified consolidation analyses employing measured consolidation parameters can also be applied. Piles, that can be driven 'drained', can be expected to remain so under any cycling that is slower than the rates applied by efficient industrial driving (perhaps 1 blow/s). Nevertheless, the kinematically constrained conditions applied at the pile–soil interface lead to the 'drained' and 'undrained' cyclic loading responses of piles driven into sand and clay, respectively, showing broadly comparable normalised cyclic shaft interaction diagrams (see Jardine, 1994).

The local shaft capacities, which are governed by the stress set up during installation, are low to the ground surface. Any significant load cycling generates two-way local failure and degradation advances from the pile head down. Stable conditions are reached if the positive effects, developing at greater depths (or load transfer to the toe), can balance the

[3]Chow (1997), Kuwano (1999) and Jardine et al. (2006) describe the Dunkerque ground properties.

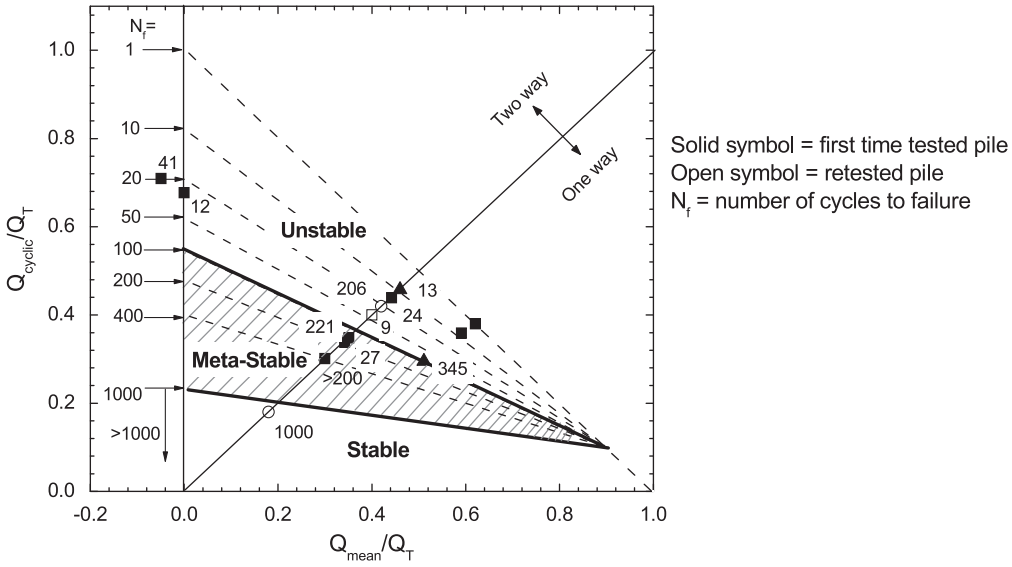


Fig. 2. Cyclic shaft failure interaction chart for full-scale piles; after Jardine and Standing (2000). *Note*: Numbers signify number of cycles developed in each test.

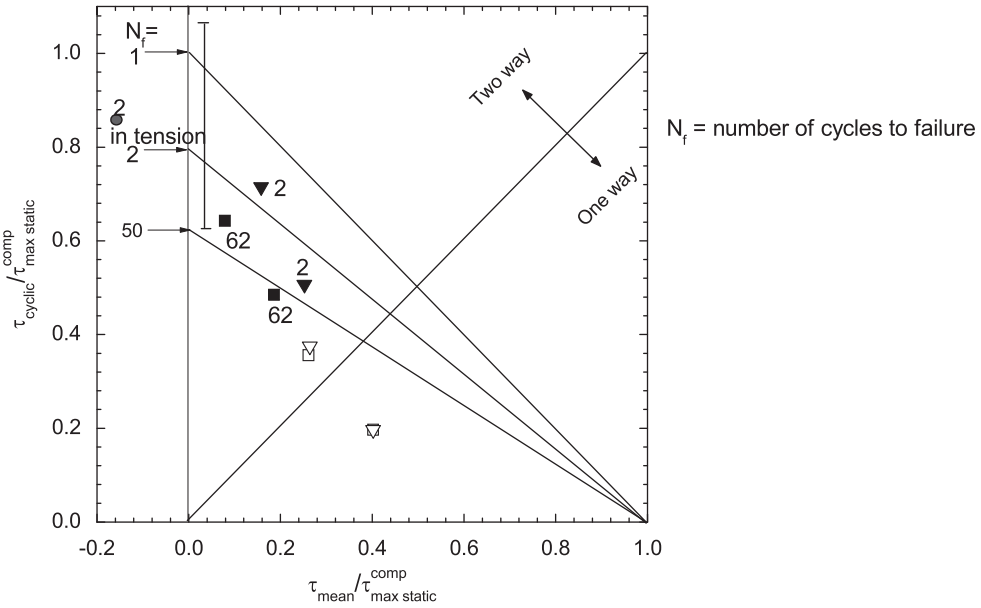


Fig. 3. Local failure cyclic interaction diagram from ICP field tests. *Where no N_f number is given in the figure the piles did not experience a cyclic failure.

losses incurred over the upper region. Model tests by White and Bolton (2004) and Yang et al. (2010) have also emphasised the importance of (i) particle crushing beneath the pile tip and (ii) a compacted interface shear zone of modified sand. The interface band identified by Yang et al. (2010) was around 20–100 grain diameters in thickness, apparently increasing with pile–soil relative displacement and the level of any applied cyclic loading. Cyclic model pile tests by Chan and Hanna (1980) found that initial tensile pre-cycling improved the subsequent performance. Poulos (1989) argued that rapid degradation commenced once the local shear displacement had exceeded that required for static failure and suggested that the effects of the loading rate may be insignificant. Al-Douri and Poulos (1994) concluded that cyclic shaft degradation becomes more pronounced as relative density increases.

The effects of time are also important. Marked gains in axial capacity over the weeks and months that follow the driving were noted by Jardine et al. (2006) in full-scale tests at Dunkerque. It was also found that high-level cycling reversed the capacity growth with time, while low-level cycling improved the shaft capacity. Le Kouby et al. (2004) noted significant gains in shaft capacity after repeated low-amplitude cycling, as did D'Aguiar et al. (2009). Chow et al. (1998) and Jardine et al. (2006) speculated that the effects of time are linked to sand creep phenomena. Bowman and Soga (2005) noted that triaxial tests involving small cyclic

perturbations accelerate the onset of volumetric dilation (which they argued accelerated set-up), while Rimoy and Jardine (2011) showed that low-level cycling systematically accelerates creep, but delays dilation. The effects of sand saturation are being explored in separate experiments, but we note that ambient pore water pressure cycling increased the 'set-up' rates in White and Zhao's (2006) small model pile tests.

The responses of sand to monotonic and cyclic shearing depend on the fabric, the initial state (void ratio and stress) and the degree of shearing of the sand (Ishihara et al., 1975). Kuwano (1999) and Kuwano and Jardine (2007) reported multiple triaxial probing and load–unload experiments that involved imposing radial effective stress paths on two types of fine silica sand and also glass ballotini. Employing highly instrumented and automatically controlled triaxial equipment, they examined a wide range of effective stress conditions, over-consolidation ratios and initial void ratios. Adopting the framework proposed by Jardine (1992) and Tatsuoka et al. (1997), which is illustrated schematically in Fig. 4, they showed that fully recoverable elastic behaviour is confined in fine silica sand to a relatively small kinematic (Y_1) yield surface. Y_1 falls within a larger nested (roughly elliptically shaped) Y_2 surface that could be inscribed (for their dense 'HRS' silica sand) in incremental $\Delta q - \Delta p'$ space by circles with radii between 0.16 and $0.33p'$. Arrival at the Y_2 surface corresponds to the 'threshold condition', noted by Vucetic (1994), that can trigger a re-direction of the strain increment vector (i.e., a change in dilatancy), the onset of markedly time-dependent behaviour and a sharp increase in the energy dissipated in load cycles. Stress paths that engage the Y_2 surface and move out towards the large scale (Y_3) yield surface show increasingly plastic and irrecoverable behaviour. While sand can either dilate or contract during Y_3 yielding, depending on its state, initially contractant (but dry of critical) samples often undergo phase transformation (PT), as defined by Ishihara et al. (1975), and start to dilate. PT takes place at stress ratios slightly below those at the critical state and dilation continues until the critical state develops. Load cycling within the Y_2 surface does not lead to significant strain accumulation, while larger amplitude cycles lead to volumetric contraction-or mean effective stress reductions in undrained tests. Extreme cycles, that engage PT, induce an initially dilatant loading response, followed by a contractant collapse upon unloading.

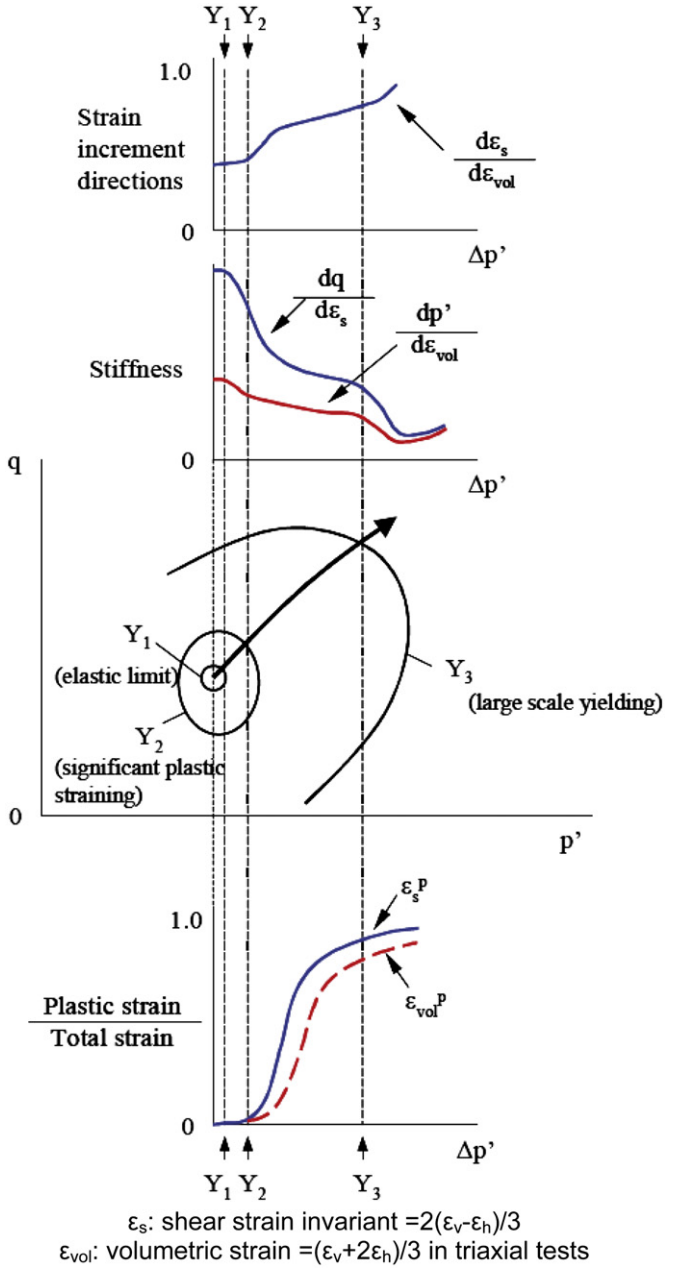


Fig. 4. Scheme of multiple yield surface (after Tatsuoka et al., 1997).

Yang et al. (2010) investigated large displacement shaft-shear behaviour through ring-shear interface tests. Constant normal stiffness (CNS) shear tests have also been proposed as pile shaft models (see Airey et al., 1992; Tabucanon et al., 1995; Fakharian and Evgin, 1997; DeJong et al., 2003, 2006; Mortara et al., 2007, 2010). A pile of radius R develops in an elastic soil a 'constrained dilation' radial stress change $\Delta\sigma_r' = 2G/R \times \Delta r$ for a radial displacement Δr caused by interface dilation or contraction, giving CNS $= \Delta\sigma_r'/\Delta r = 2G/R$ (Jardine et al., 2005). Static CNS tests tend to dilate, while cyclic experiments invariably compact with normal effective stress and shear capacity reduced with N. Representative CNS tests require specimen fabrics resembling those around pile shafts and normal stiffness that matches the field values. G varies with state, strain level and loading conditions, while CNS also varies inversely with R, making matching difficult. However, constant volume shear tests, with infinite CNS, provide useful upper bound predictions of potential cyclic effects that also match the conditions applied during undrained loading in saturated soil (Jardine et al., 2005).

1.2. Suitability of CC tests to study pile–soil stress conditions

The experiments were designed to gain a fundamental understanding by (i) making local effective stress

measurements on and around piles undergoing cyclic loading, (ii) linking the response observed to the stress–strain behaviour of the sand and (iii) covering the three styles of cyclic responses outlined in Fig. 2. Calibration chambers (CCs) present a number of advantages for such a study, as well as some drawbacks. The control CCs offer over-sand placement and the boundary stress makes them the standard tool for calibrating CPT devices. The adopted instrumentation scheme allowed the contact stress on the pile shafts and the local vertical, radial and circumferential stress (σ_z' σ_r', and σ_θ') in the surrounding soil mass to be measured, which would not be feasible in the field. The selected pile and soil stress sensor dimensions have ratios with respect to the sand grain size that exceed the limits suggested by Bolton et al. (1999) and Zhu et al. (2009). The chamber-to-pile diameter ratio (33.3) is also adequate, although higher multiples may be required to fully match it to that in the field (Salgado et al., 1998). While the INPG CC boundary conditions offer a good match for field penetration far below the ground level, they do not represent the conditions near the ground surface as well, or they offer the multi-gravity scaling of centrifuge experiments. As with any reduced scale model, the interface shear band (the thickness of which is defined by grain size), that develops around the shaft, may lead to particle-to-pile ratio scale effects. While adopting dry sand enables the avoidance of all pore pressure considerations, excess pressure would not be expected with saturated clean sand. In addition, as discussed above, drainage may not be of primary importance during cyclic loading because of the highly kinematically constrained interface boundary conditions. However, the scalar dependence of the dissipation rates would have to be considered carefully when testing lower permeability soil and it would be difficult to match the field pore pressure in many cases.

2. Testing arrangements and programme

The procedures applied to deploy the instruments, fill the chamber and conduct the tests are described fully by Jardine et al. (2009) and Zhu et al. (2009), who also report on the design of the CC, Mini-ICPs and all the instrument calibrations. We briefly summarise the information below.

2.1. INPG environmentally-controlled calibration chamber

The general arrangement is illustrated in Fig. 5. The chamber is 1.5 m high, 1.2 m in internal diameter and has a rigid base and top. An upper membrane applies vertical stress, which was maintained at ~150 kPa throughout the tests. A lubricated latex membrane reduced the wall friction between the sand and the tank. As noted in the ICP field tests referred to earlier, the stress developing around the penetrating pile, at any soil depth, varies directly with local cone resistance q_c and inversely with relative tip depth h/R. It also varies with radial distance r/R from the pile axis (see Jardine et al., in press, under review).

2.2. Fontainebleau NE34 sand

The CC was filled with industrially prepared, silt-free, NE34 sand whose index parameters are given in Table 1. The pluviation system described by Jardine et al. (2009) was adjusted to give $e_0=0.62$, or a relative density of $D_r=72\%$. Separate CPT tests were conducted under $\sigma_{vo}' = 150$ kPa to match the various

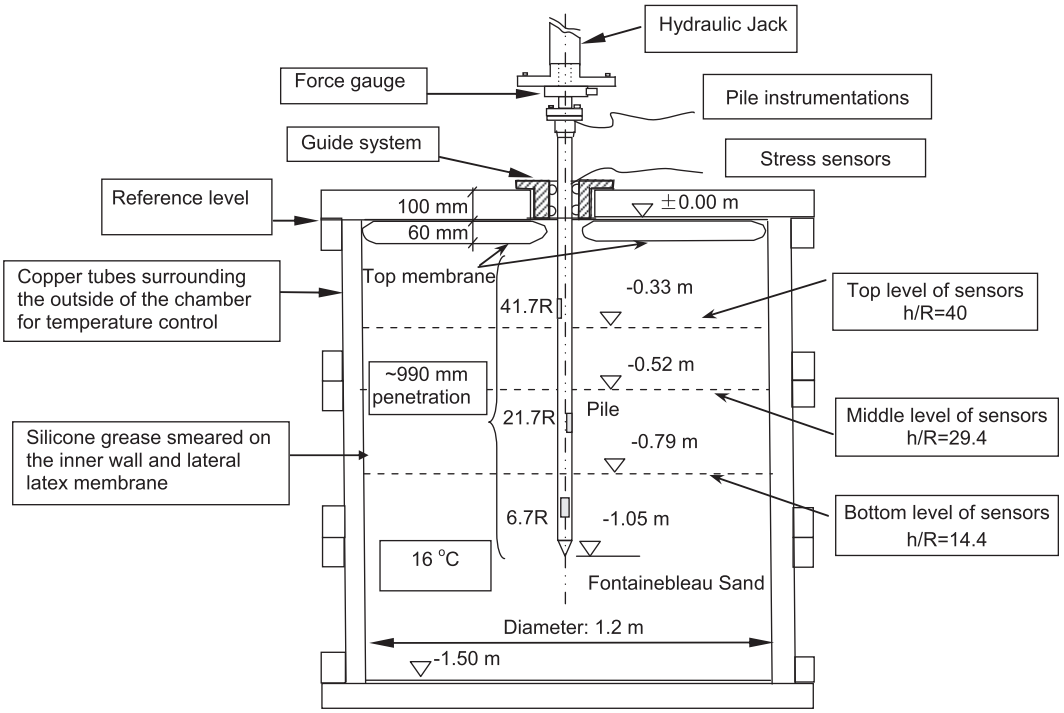


Fig. 5. Typical general arrangements for Mini-ICP tests.

Table 1
Fontainebleau NE34 sand.

Grain shape	D_{10} (mm)	D_{50} (mm)	D_{60} (mm)	e_{max}	e_{min}
Sub-angular	0.15	0.21	0.23	0.90	0.51

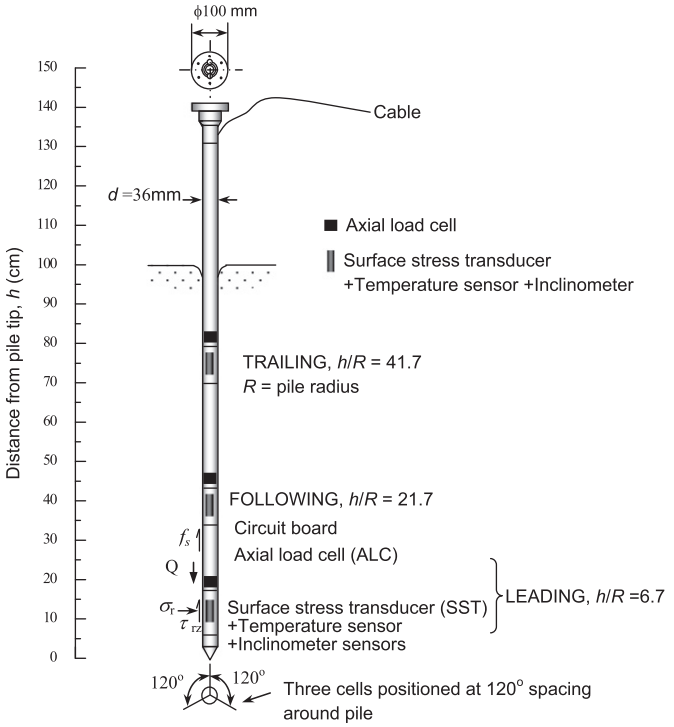


Fig. 6. Typical Mini-ICP1 configuration.

CC configurations. While the test profiles depended on the details of the boundary conditions, all developed $q_c = 21 \pm 2$ MPa in the main mass. Yang et al. (2010) and Altuhafi and Jardine (2011) provided details of the soil properties. Triaxial and shear box tests (conducted under $100 < \sigma'_n < 500$ kPa with $e_0 = 0.62$) showed peak and critical state $\varphi' \approx 35^\circ$ and 33°, respectively. Lower φ' values and contractive behaviour were noted in high-pressure triaxial compression tests that reproduced the particle breakage caused by the advancing pile tip. The heavily fractured and pre-stressed interface shear zone soil, which contains up to 15% silt, showed notably higher φ' and stronger dilation when re-sheared after unloading. Ring-shear interface tests that reproduce the interface conditions showed δ' values between 25° and 27°.

2.3. Imperial College Mini-ICP pile

The closed-ended stainless steel Mini-ICP pile, 36 mm in diameter, comprises Leading, Following and Trailing instrument clusters with a 60° conical tip, as shown in Fig. 6. Mini-ICPs 3 and 4 included an extra cell to isolate tip resistance. Each cluster contains a temperature sensor, an inclinometer, an axial load cell and a very stiff surface stress transducer (SST) to measure the radial total stress (σ_r) and the shear stress (τ_{rz}). The SSTs can follow the local stress paths during installation, equalisation and load testing; they are considered insensitive to the effects of cell action (Jardine et al., 2009).

2.4. Soil stress sensors

Breaks were made during sand pluviation to install dozens of pressure sensors, from 0.6 to 1.4 mm in thickness and from 6 to 6.5 mm in diameter (manufactured by TML and Kyowa) at either two or three levels in the CC sand mass. A laser and precision-made template system guided the accurate positioning of the cells at prescribed radial positions (with $2 \le r/R \le 20$), as described by Jardine et al. (2009). The strain-gauged, miniature diaphragm normal stress cells, their calibration characteristics and data reduction routines are described by Zhu et al. (2009). The cells were oriented in the direction of the stress (σ'_z, σ'_r or σ'_θ) to be measured. Careful calibrations were required to address the considerable cell action factors and markedly non-linear in situ responses shown by these cells.

2.5. Installation

A fresh sand-filled chamber was prepared for each of the four Mini-ICP pile installations. There were slight variations in the boundary conditions adopted for each test. Separate installations were made with matching boundary conditions for parallel CPT tests, which provided case specific q_c traces that were used to normalise the measured soil and pile stress (Jardine et al., in press). The sand masses were stabilised under $\sigma'_z = 150$ kPa for up to five weeks prior to each installation. The four Mini-ICPs were installed with jacking cycles that simulated the aspects of driving by applying stroke lengths between 5 and 20 mm, with the pile head loads decreasing to zero at the end of each stroke. The rates of advance were around 0.5 mm/s. The final tip depths were 0.92 m below the sand surface for Mini-ICP1 and 0.99 m for the other three installations.

Jardine et al. (in press, under review) assessed the stress state around the shaft by adding τ_{rz} stress components, projected from the pile instruments assuming the classical inverse variation with radius, to the direct measurements:

$$\tau_{rz} = [\tau_{rz}]_{r=R} R/r \tag{1}$$

Then,

$$p' = \tfrac{1}{3}(\sigma'_1 + \sigma'_2 + \sigma'_3) \tag{2}$$

$$q = \frac{1}{\sqrt{2}} \sqrt{(\sigma'_1 - \sigma'_2)^2 + (\sigma'_3 - \sigma'_2)^2 + (\sigma'_2 - \sigma'_1)^2} \tag{3}$$

$$\sigma'_1 = \frac{\sigma'_r + \sigma'_z}{2} + \sqrt{\left(\frac{\sigma'_r - \sigma'_z}{2}\right)^2 + \tau_{rz}^2} \tag{4}$$

$$\sigma'_2 = \sigma'_\theta \tag{5}$$

$$\sigma_3' = \frac{\sigma_r' + \sigma_z'}{2} - \sqrt{\left(\frac{\sigma_r' - \sigma_z'}{2}\right)^2 + \tau_{rz}^2} \quad (6)$$

The stress regime, close to the pile shaft before static testing, was interpreted by Jardine et al. (under review) as showing σ_r' approximately mid-way between σ_θ' and σ_z', allowing mean effective stress p' to be estimated as being approximately equal to the measured σ_r'. Considering the incremental form of (6), as applied in calculations of elastic stiffness response, we note that the pre-Y_2 shaft loading changes that alter τ_{rz} alone lead to equivalent incremental changes (defined relative to a local stress origin) of $\Delta q = \sqrt{3}\Delta\tau_{rz}$.

2.6. Load testing

Multiple static and cyclic tests were conducted after each Mini-ICP installation into a fresh sand mass to extend the scope of the investigation. Recognising that age and prior testing affect the static and cyclic capacity (Jardine et al., 2006), static tension tests were carried out between each cyclic experiment to track Q_T. Jardine and Standing (2000) found that normalising the cyclic loading levels, by applying Q_T just before cycling, largely eliminates the effects of the loading history in their full-scale field tests; this feature was assumed to apply to the Mini-ICP model experiments. The static tests were programmed to run with rates of axial displacement (s) fixed at $ds/dt = 0.01$ mm/s. The first were conducted from 41 to 139 day after the installation. To reduce the testing 'damage', the displacements were limited to the minima required to define failure: $s < 3.6$ mm or $0.1D$. The initial capacities and the local radial stress trends with h/R were broadly compatible with the predictions made with the ICP field design procedures (Jardine et al., 2005), thus indicating trends that are broadly representative of the field behaviour.

2.7. Cyclic testing

Cyclic loading was applied through a Rosier electrically controlled jacking system that could apply sinusoidally varying pile head loads or displacements. Table 2 summarises the cyclic testing programme, giving the loading parameters for each experiment normalised by the evolving Q_T listed in Table 3. The first tensile one-way (OW) load-controlled cyclic experiments were conducted after the initial static tests, which were followed by alternating static tensile capacity (Q_T) tests and cyclic experiments involving a range of (OW, TW, load

Table 2
Mini-ICP cyclic loading conditions; normalising tension capacities are given in Table 3.

Installation	Cyclic test	N cycles applied	Control mode	Mean cyclic period T (min)	Q_{cyclic}/Q_T	Q_{mean}/Q_T
Mini-ICP1	ICP1-OW1 Meta-stable	1000	Load control: from 0 to −4.0 kN	0.58	0.22	0.22
	ICP1-TW1 Unstable	100 (N_f=4)	Displacement control From −4 to +5 mm per cycle	2.64	0.41	0.06
Mini-ICP2	ICP2-OW1 Stable	1000	Load control: from 0 to −3.0 kN	0.43	0.12	0.12
	ICP2-OW2 Stable	1000	Load control: from 0 to −4.8 kN	0.70	0.20	0.20
	ICP2-OW3 Meta-stable	500	Load control: from 0 to −6.8 kN	1.04	0.28	0.28
	ICP2-TW1 Unstable	100 (N_f=4)	Displacement control From −2 to +3 mm per cycle	2.17	0.48	0.15
Mini-ICP3	ICP3-OW1 Unstable	100 (N_f=66)	Load control: from 0 to −9.6 kN	1.64	0.38	0.38
	CP3-TW1 Unstable	1 (N_f=1)	Load control: from −5.0 kN to +8.0 kN (shaft load: −5–6.67 kN)	6	0.54	-0.08
	ICP3-TW2 Unstable	199 (N_f=165)	Load control: from −5.0 kN to +5.0 kN (shaft load: −5–3.80 kN)	0.73	0.40	0.06
	ICP3-TW3 Unstable	50 (N_f=10)	Load control: from −5.0 kN to +7.0 kN (shaft load: −5.0–4.65 kN)	1.04	0.44	0.02
	ICP3-TW4 Unstable	37 (N_f=3)	Load control: from −5.0 kN to +10.0 kN (shaft load: −5.0–4.53 kN)	2.16	0.44	0.02
Mini-ICP4	ICP4-OW1 Stable	7000	Load control: from 0 to −3.5 kN	0.43	0.15	0.15
	ICP4-TW1 Meta-stable	600 (N_f=580)	Load control: from −4.0 kN to +4.0 kN (shaft load: −4.0–2.4 kN)	0.44	0.23	0.06
	ICP4-OW2 Meta-stable	50 (Test incomplete)	Load control: from −2.3 to −4.6 kN	0.18	0.21	0.63

Note: OW=one-way tension test; TW=two-way compression/tension test.
Definitions of Q_{cyclic}, Q_{mean} and Q_T: see Fig. 1.

Table 3
Static tension tests performed after each cyclic test.

Test	ID	Prior test: see Table 2	Tension capacity, Q_T (kN)
Mini-ICP1	ICP1-T1	1st Compression test	9.2
	ICP1-T2	ICP1-OW1	10.8
	ICP1-T3	ICP1-TW1	4.9
Mini-ICP2	ICP2-T1	1st Compression test	12.1
	ICP2-T2	ICP2-OW1	13.2
	ICP2-T3	ICP2-OW2	14.0
	ICP2-T4	ICP2-OW3	13.7
	ICP2-T5	ICP2-TW1	8.7
Mini-ICP3	ICP3-T1	1st Compression test	12.5
	ICP3-T2	ICP3-OW1	10.9
	ICP3-T3	ICP3-TW1,2,3,4	4.8
Mini-ICP4	ICP4-T1	1st Compression test	11.5
	ICP4-T2	ICP4-OW1	13.9
	ICP4-T3	ICP4-TW1	5.5
	ICP4-T4	ICP4-OW2	6.0

and displacement control) configurations. Following the scheme given in Fig. 1, pile head load amplitudes $Q_{cyclic}=(Q_{max}-Q_{min})/2$ varied from low levels up to 40% of the pre-test tension shaft capacity Q_T, while $Q_{mean}=(i_{max}+Q_{min})/2$ ranged from -0.08 to 0.63 (where Q_{max} and Q_{min} are the maximum and minimum shaft loads, respectively). Tensile shaft loads are considered negative and the cyclic frequencies ranged between 0.5 and 2.5 cycles/min for the high-level and the extended low-level tests, respectively.

The tip loads are negligible under static or OW tensile cyclic tests, so in these cases the shaft load was effectively equal to the pile head load. Tip forces were deducted from pile head loads to give shaft loads from static and cyclic experiments that involved compressive loading. Direct tip force measurements were made with Mini-ICPs 3 and 4, while less accurate projections were made for Mini-ICP 1 and 2 from load cells positioned at three higher shaft levels. Two-way loading was applied in later tests under both load and displacement control. Naturally, pile head loads can change during displacement controlled tests, in which the shaft-to-toe load split also shows more variation. For simplicity, Table 2 lists the average shaft cyclic loading parameters applied over each test.

Cyclic failure was identified in any test where: (i) accumulated displacements (s) reached 10% of the pile diameter (i.e., 3.6 mm), or (ii) rates ds/dN showed a sharp increase (that is d^2s/dN^2 rose markedly). Displacement rates ds/dN are considered *slow*, if less than 1 mm/10^4 cycles, or *fast*, if more than 1 mm/100 cycles.[4] The response is then

- *Stable* if no failure develops before $N=1000$, with slow and reducing rates of permanent displacements.
- *Unstable* if failure occurs with $N<100$.
- *Meta-Stable* if failure develops with $1000>N>100$, or if permanent displacement rates fail to stabilise at slow values.

[4]These rates should be scaled by pile diameter before being applied to differently sized piles.

3. Observed behaviour

As identified in Table 2, the 14 cyclic experiments exhibited a range of *Stable*, *Meta-Stable* and *Unstable* cyclic behaviours. Fig. 7 illustrates the responses by plotting the 'average' loading parameters normalised by the Q_T values measured prior to the cyclic tests, adopting the same approach as the field tests presented in Fig. 2. The tentative pattern of zone boundaries indicated in Fig. 7 is broadly comparable to that shown by the field tests in Figs. 2 and 3.

We review below the detailed measurements, considering the response categories separately and relating the observations to the key features of sand behaviour.

3.1. Stable Zone

The three stable tests all showed slow permanent displacement rates that increased systematically with Q_{cyclic}/Q_T. Examples of the *Stable* load–displacement loops and cumulative displacements (*ICP2-OW1 and ICP4-OW1* with $Q_{cyclic}=Q_{mean}$) are given in Figs. 8 and 9. Stable responses are expected under the broader range of conditions identified in Fig. 7. One slightly more highly loaded test, *ICP1-OW1*, just exceeded the critical 1 mm/10^4 cycle displacement rate and so helped to define the lower Meta-Stable Zone boundary. Table 3 shows that tension capacities grew by up to 20% after extended Stable cycling, as also illustrated in Fig. 10, where the changes in tension capacity (ΔQ_T) before and after each particular stage of cycling are shown normalised by Q_T and plotted against Q_{cyclic}/Q_T.

Illustrations of how the local stress developed at the leading pile instrument cluster are presented for the same exemplar tests in Fig. 11, showing broadly stable trends. Further information from these tests is given for all Mini-ICP sensor positions in Fig. 12, plotting the local interface shear stress paths. The leading cell shows nearly closed, almost linear, loops with negative $d\tau_{rz}/d\sigma_r'$ gradients. The trailing and following SST's loops become broader and migrate further to the left (σ_r' reducing) with increasing N. While the paths remain within the $\delta'=27^\circ$ interface shear test envelope, the trailing SST paths traverse the greatest peak-to-trough mobilised δ' range. The traces show the expected tendency for minor cyclic degradation to creep top downwards and be stabilised by load carrying capacity improving over the lower segment of the shaft.

Estimates are shown in Fig. 12 of the limits in $\tau_{rz}-\sigma_r'$ stress space to the initial Y_2 surfaces defined in Fig. 4. These were estimated from Kuwano and Jardine's (2007) results for medium dense silica sand. Over the stress range considered, the limits in incremental $\Delta q-\Delta p'$ space can be estimated as ellipses that can be inscribed around the

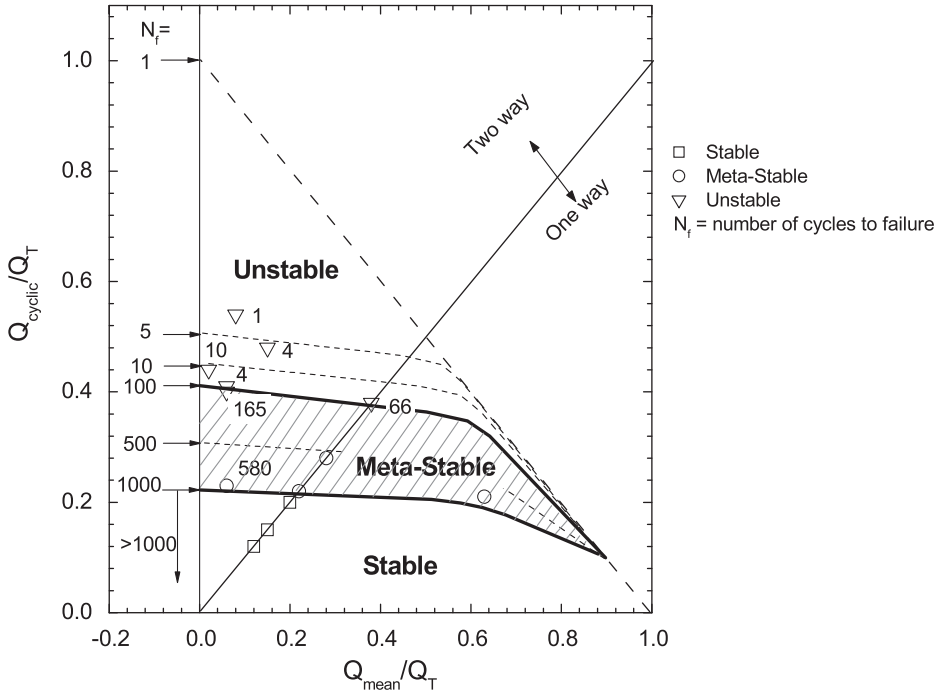


Fig. 7. Summary of average cyclic shaft loading and failure conditions in Mini-ICP tests, showing tentative *Stable*, *Meta-Stable* and *Unstable* Zone boundaries. *Where no N_f number is given in the figure the piles did not experience a cyclic failure.

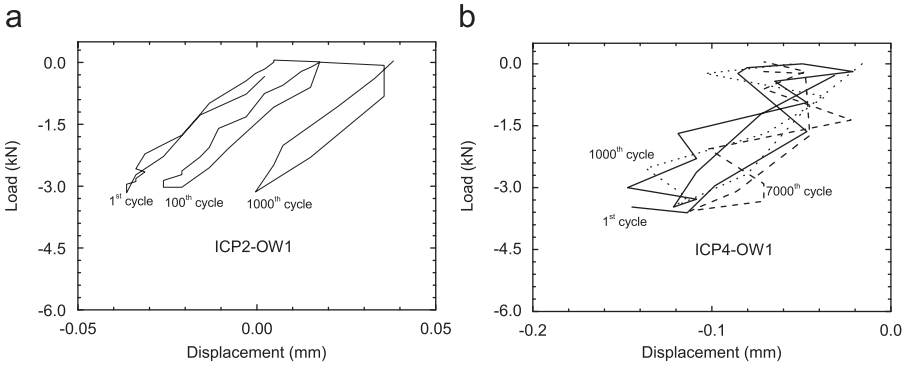


Fig. 8. Force–displacement behaviour of example *Stable* tests.

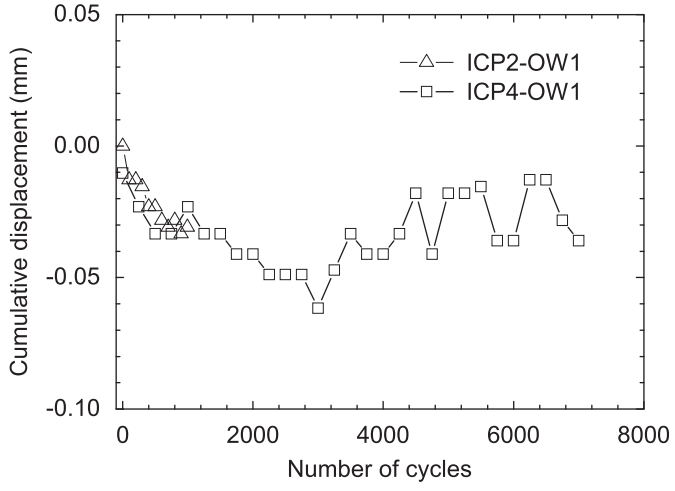


Fig. 9. Cumulative displacements for example *Stable* tests.

current effective stress point by circles with radii from 0.16 to $0.33p'$. Taking the average radius, applying Eqs. (3)–(6) and noting from Jardine et al. (under review) that σ_r' may be approximately equal to p' close to the shaft, leads to approximate estimates for the vertical (maximum-to-minimum) Y_2 surface limits applied under pure shaft shear loading of $\Delta\tau_{rz}/\sigma_r' \sim 0.28$. While this estimate should be checked for NE34 sand, through tests conducted under matching loading conditions, it does allow indicative envelopes to be plotted in Fig. 12. The stress paths followed at the leading and the following shaft levels remain well within the 'lower-bound' Y_2 limits and do not migrate significantly during cycling. However, the shallowest, trailing cluster's paths may engage Y_2 yielding and initiate a contractant response. The effective stress paths start to migrate to the left without meeting the $\delta' = 27^\circ$ lines or any slip developing. The effective stress

paths (and subsequent load tests) show (i) modest top-down degradation and (ii) prove that the tensile capacity gains shown in Fig. 10 are not due to gains in σ_r' or δ'. Instead, they are interpreted as being due to the marginal densification of the interface zone and the development of an optimal soil fabric that enhances dilation under static loading.

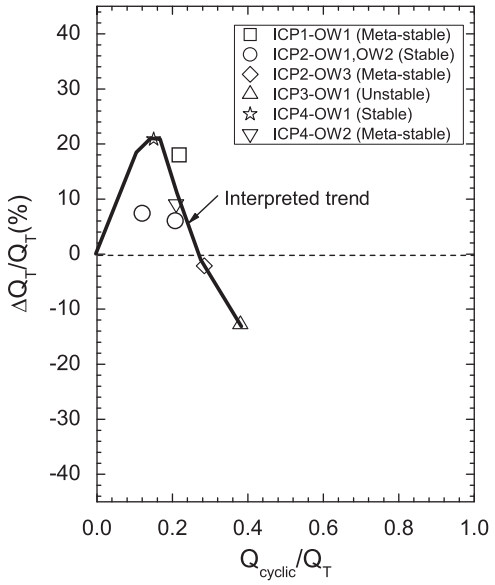


Fig. 10. Effect of load cycling on tensile capacity in one-way tests.

Fig. 13 illustrates the corresponding soil mass's effective stress paths, considering the $r/R=5$, $h/R\approx 15$ location. Also shown is an estimate for the initial Y_2 kinematic yield surface, with a circle of radius $0.245p'$ representing the mid-point in the $0.16–0.33p'$ range noted from Kuwano and Jardine's (2007) triaxial tests. The paths are generally stable, sub-vertical and remain well away from the estimated Y_2 yield surface and failure envelope.

3.2. Meta-Stable Zone

The four Meta-Stable experiments cover a wide sweep in Fig. 7. Their load–displacement loops tended to broaden and the permanent displacement rates accelerated, as shown in Figs. 14 and 15 by ICP2-OW3, ICP4-TW1 and ICP4-OW2, examples that span the range of marginally *Meta-Stable* to nearly *Unstable*. Two-way tests could reverse their displacement trends, with an initial tendency to gradually settle, changing to a pull-out cyclic failure, as seen in the field by Jardine and Standing (2000). The single OW tests, conducted with $Q_{cyclic}/Q_T > 0.25$, led to reductions in tensile shaft capacity in place of the gains seen under lower cyclic levels (see Fig. 10). Table 3 shows that the capacities tend to fall still further in tests that impose higher cyclic loading levels.

The local shaft stress, developing at the leading SST, is illustrated for the two exemplar tests in Figs. 16 and 17. The effective stress paths all appear to engage the estimated initial kinematic Y_2 surfaces, developing clearly

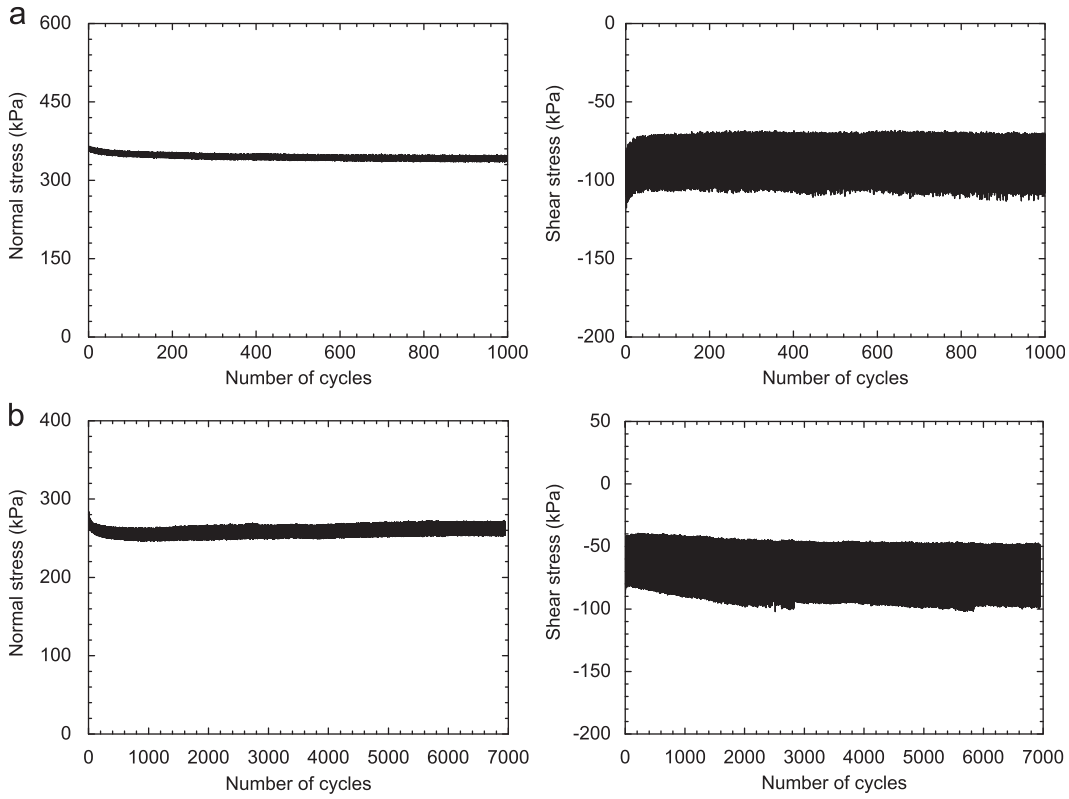


Fig. 11. Shear and normal stresses at leading SST cluster during example *Stable* tests. (a) ICP2-OW1 and (b) ICP4-OW1.

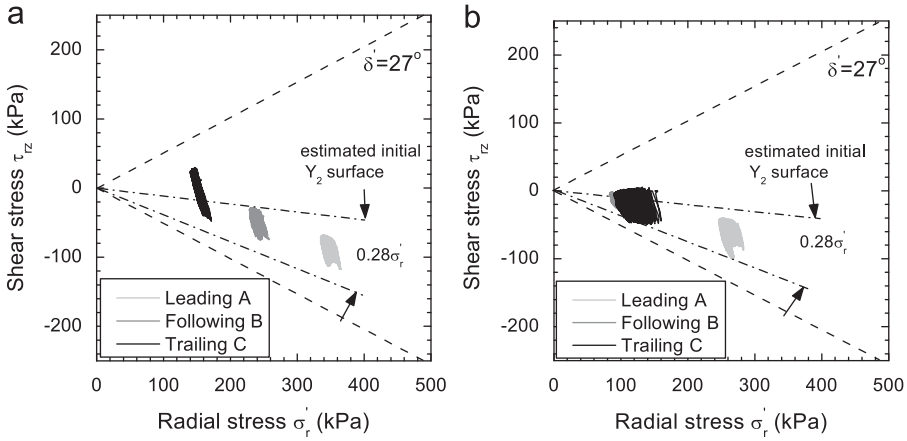


Fig. 12. Effective stress paths at all SSTs during example *Stable* tests. (a) ICP2-OW1 and (b) ICP4-OW1.

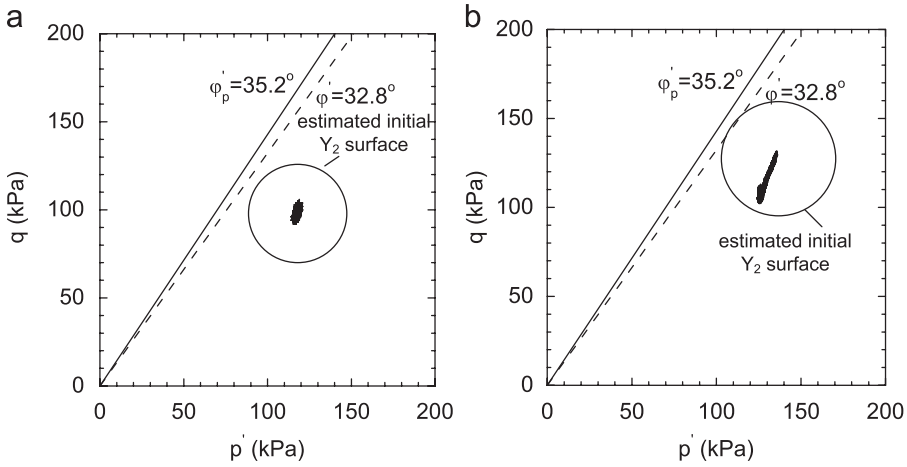


Fig. 13. Effective stress path developed in sand mass at $5R$, $h/R \approx 15$ during example *Stable* tests. (a) ICP2-OW1 and (b) ICP4-OW1.

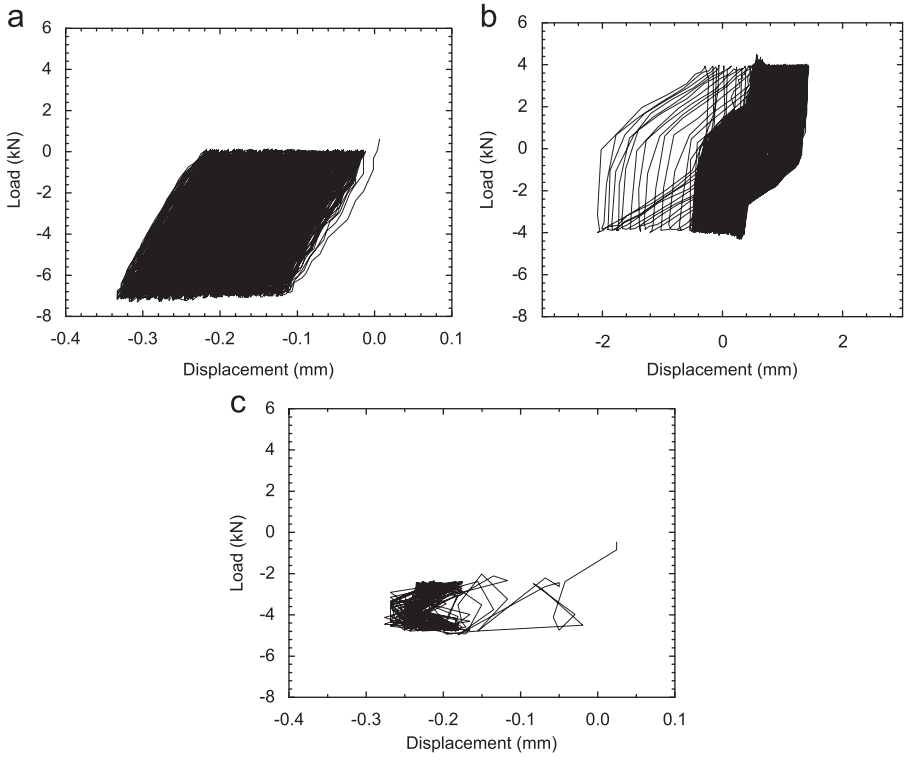


Fig. 14. Force–displacement behaviour of example *Meta-Stable* tests. (a) ICP2-OW3, (b) ICP4-TW1 and (c) ICP4-OW2.

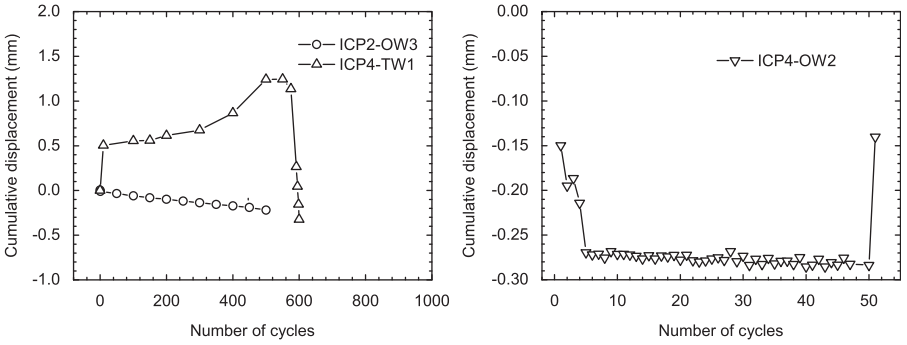


Fig. 15. Cumulative displacements of example *Meta-Stable* tests.

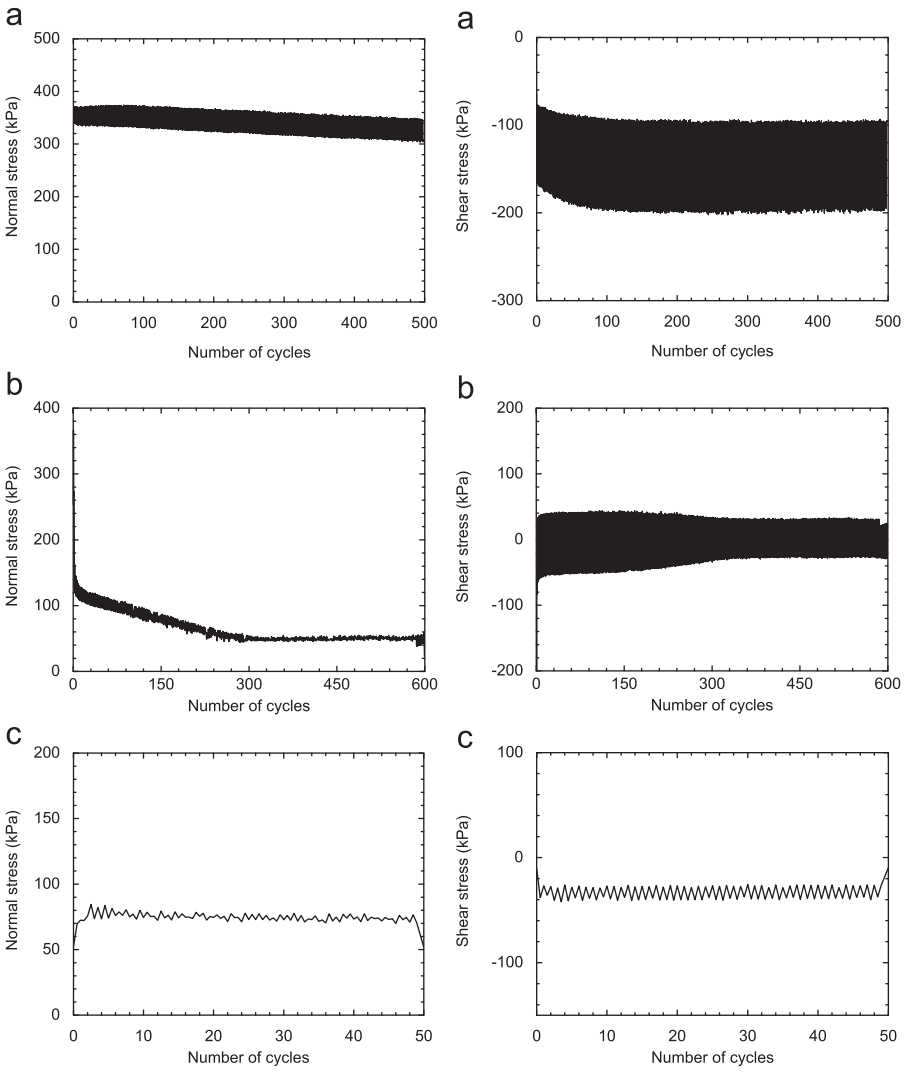


Fig. 16. Shear and normal stresses at leading SST cluster during example *Meta-Stable* tests. (a) ICP2-OW3, (b) ICP4-TW1 and (c) ICP4-OW2.

contractive paths that gradually approach the interface failure envelope. The patterns depend on the loading style, being asymmetrical under OW conditions and more symmetric under TW conditions. The trailing cells show the most marked cyclic migration (σ_r' reducing) and the greatest peak-to-trough range in mobilised δ', confirming again a top-down failure. The OW tests follow negatively inclined effective stress paths that do not engage phase transformation. However, the more severely loaded TW tests undergo phase transformation (PT) and dilate to climb the interface failure line, developing ''butterfly wing'' patterns (see ICP4-TW1) in which each dilatant 'loading' stage is followed by sharp contraction on 'unloading'. Any densification within the interface shear zone allows radial

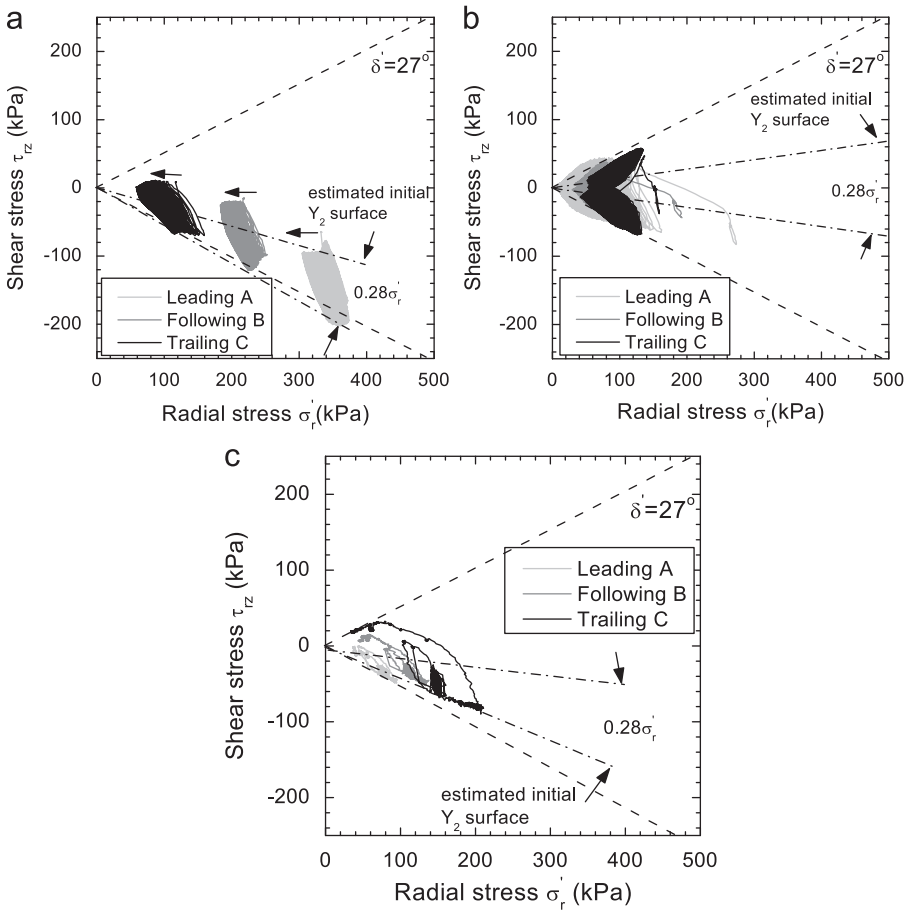


Fig. 17. Effective stress paths at all SSTs during example *Meta-Stable* tests. (a) ICP2-OW3, (b) ICP4-TW1 and (c) ICP4-OW2.

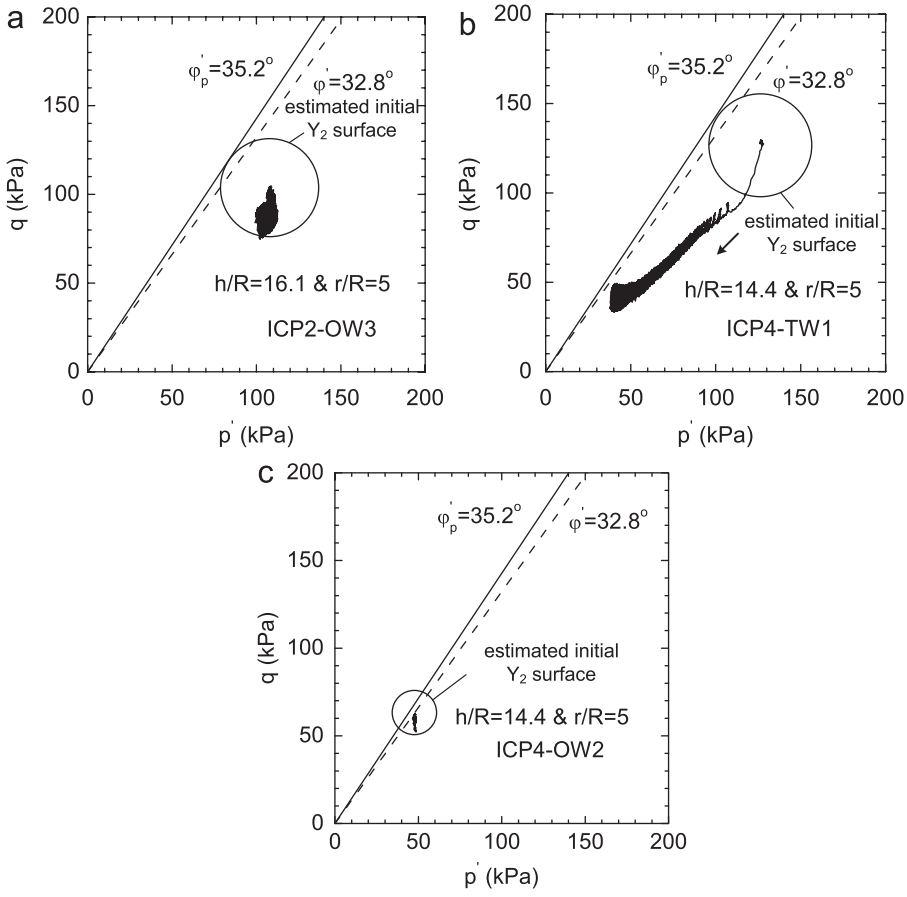


Fig. 18. Effective stress paths developed in sand mass at $5R$, $h/R \approx 15$ during example *Meta- Stable* tests. (a) ICP2-OW3, (b) ICP4-TW1 and (c) ICP4-OW2.

stress to relax, as described earlier. The resulting local shaft capacity loss and interface slip leads, in the TW tests, to the transfer of compressive load from the shaft to the pile tip.

Fig. 18 illustrates the corresponding effective stress paths within the soil mass at the $r/R=5$, $h/R\approx 15$ location, again with the estimated initial Y_2 yield surfaces shown for reference. Slowly moving sub-vertical loops develop in

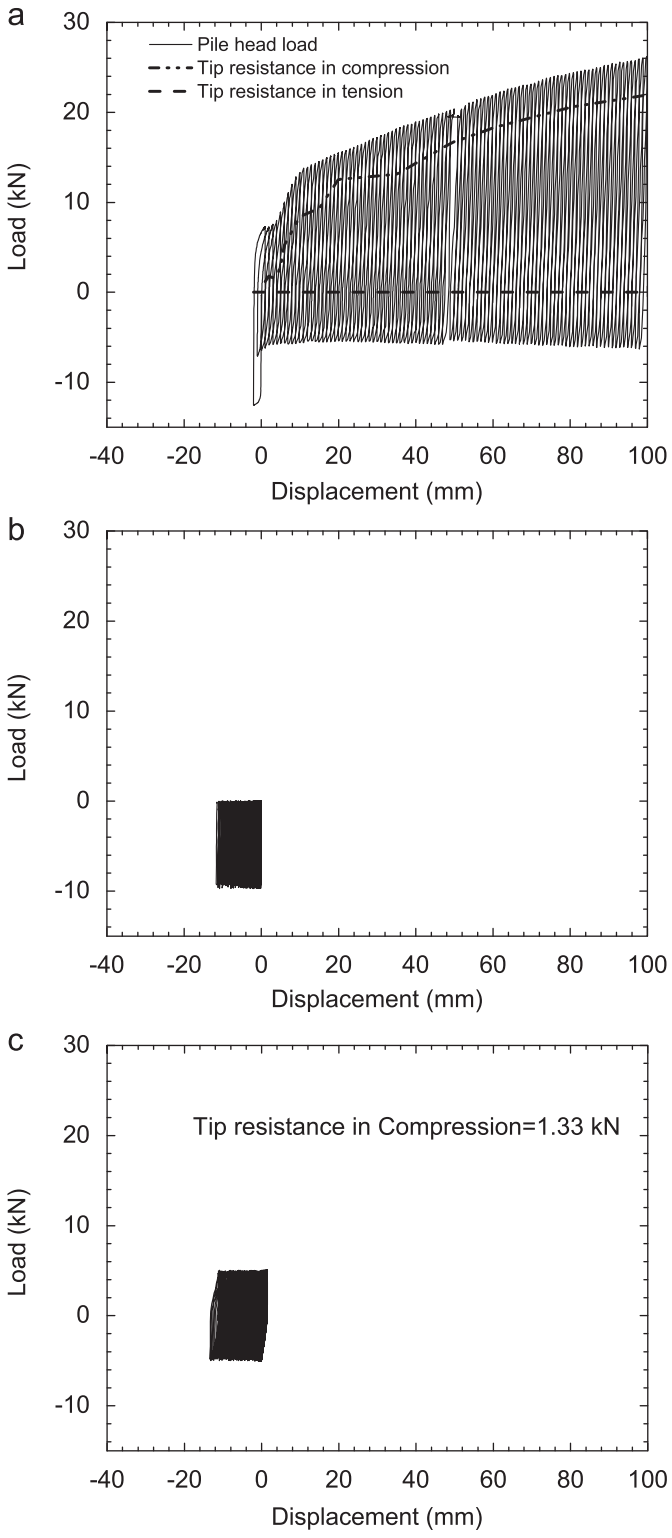


Fig. 19. Force–displacement behaviour of example *Unstable* tests. (a) ICP2-TW1, (b) ICP3-OW1 and (c) ICP3-TW2.

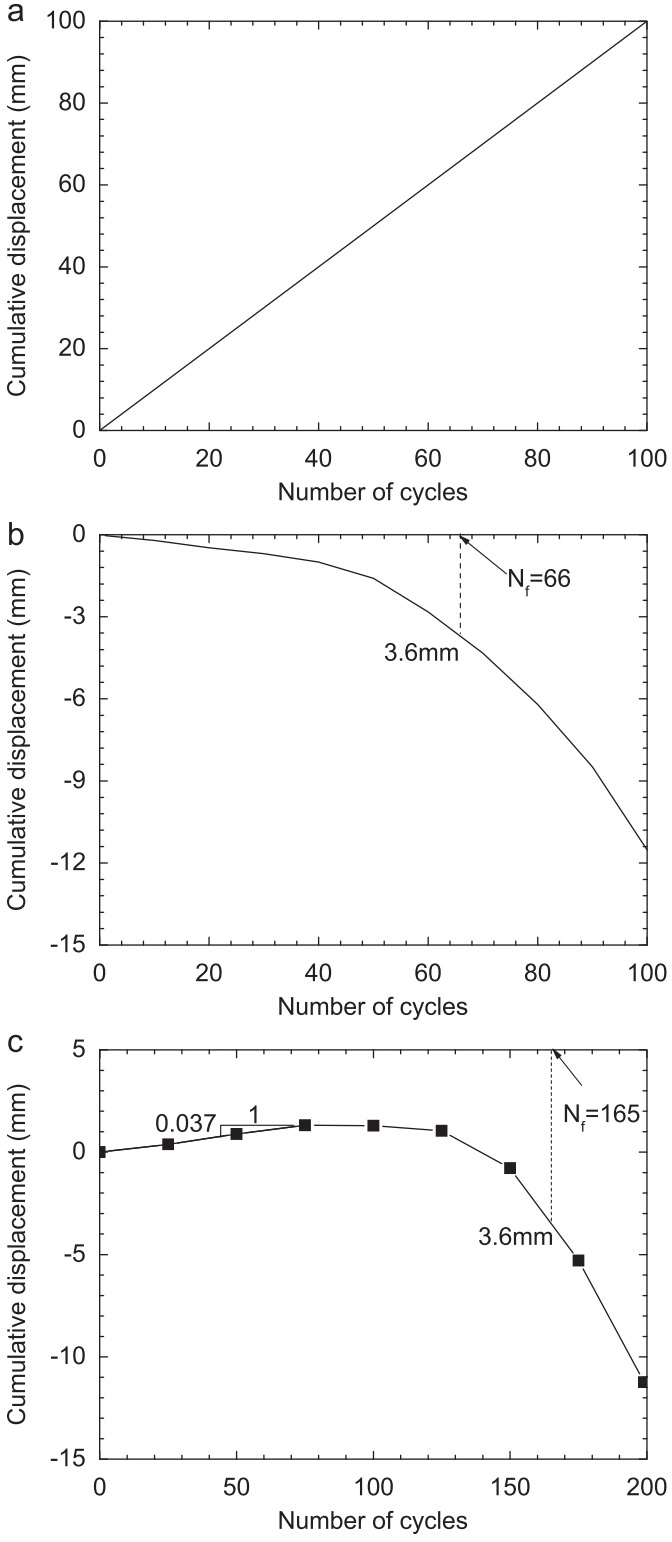


Fig. 20. Cumulative displacements for example *Unstable* tests. (a) ICP2-TW1, (b) ICP3-OW1 and (c) ICP3-TW2.

marginally *Meta-Stable* cases (ICP2-OW3 and ICP4-OW2) that may or may not engage the estimated Y_2 surfaces, but the more heavily loaded ICP4-TW1 follows a path that migrates strongly to the left and to overall failure. The p' reductions are interpreted as being principally due to contraction in the kinematically controlled interface shear zone.

3.3. Unstable Zone

The seven *Unstable* tests are all plotted in the upper left portion of Fig. 7, although unstable responses are likely over the broader sweep indicated. The figure plots the tests' average loading parameters; note that ICP1-TW1 and ICP2-TW1 were displacement-controlled to 'fail continuously' in both compression and tension, penetrating progressively by 1 mm per cycle; both were started by imposing $Q_{cyclic} \approx Q_T$. Some examples of *Unstable* force–displacement behaviour are shown in Fig. 19, which identifies the shaft and base trends for ICP2-TW1. The latter test showed the overall 'capacity' reduction over the first few cycles, and then the picking up of compression as the tip response stiffened and the base loads climbed. The shaft capacities either fell, or remained roughly stable, until settling (from $N=100$) at around half of their initial values. The five other *Unstable* experiments, ICP3-OW1, ICP3-TW1, ICP3-TW2, ICP3-TW3 and ICP3-TW4, were load-controlled and retained relatively steady and low (<1.3 kN) tip load maxima throughout. Fig. 20 reports three cases of the displacement–time styles, including the reversal of sign in ICP3-TW2 after 10 cycles. Table 3 details the impact of Unstable cycling on the tension shaft capacity.

The local shaft stress recorded at the leading SSTs varied substantially during unstable cycling. The three example tests involved interface failure where, as shown in Figs. 21 and 22 the effective stress paths moved sharply to the left (σ_r' reducing) and engaged a δ' limit similar to the 27° seen in ring-shear tests. All *Unstable* tests engaged the Y_2 surfaces at early stages of their first cycle and proceeded to contract markedly before undergoing interface phase transformation (PT). The post-PT paths climbed the interface failure line during both forward and reverse pile slip stages, collapsing after each to develop "butterfly wing" patterns. In most cases, the failure was nearly symmetrical. However, *Unstable* tests run with higher Q_{mean}/Q_T ratios developed asymmetric effective stress paths, as in ICP3-OW1.

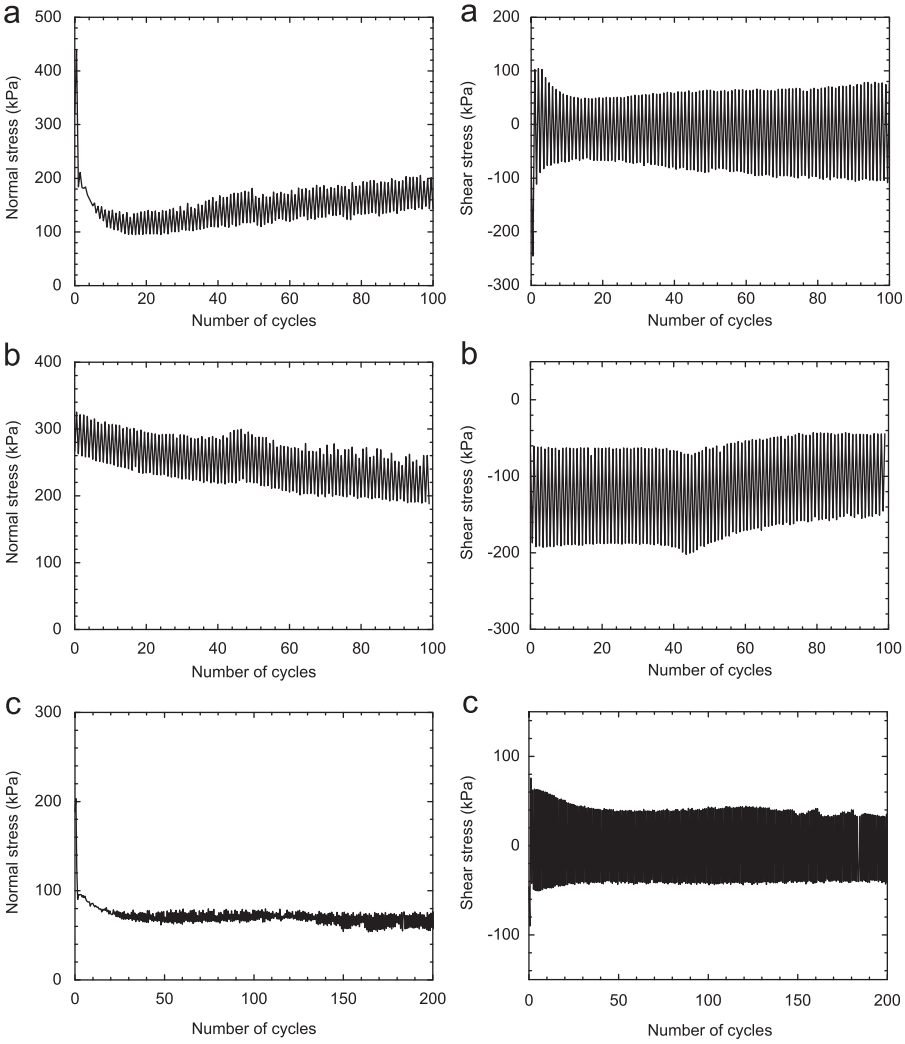


Fig. 21. Shear and normal stresses at leading SST cluster during example *Unstable* tests. (a) ICP2-TW1, (b) ICP3-OW1 and (c) ICP3-TW2.

The corresponding effective stress path plots for the $r/R=3$, $h/R \approx 15$ location, presented in Fig. 23, all engaged their Y_2 surfaces at early stages and subsequently migrated strongly to the left. The sand mass was neither behaving elastically, nor providing a steady normal stiffness around the shaft. Cyclic degradation was developing as a combined effect of plastic behaviour in the soil mass and the gradually thickening and fracturing interface shear zone (Yang et al., 2010).

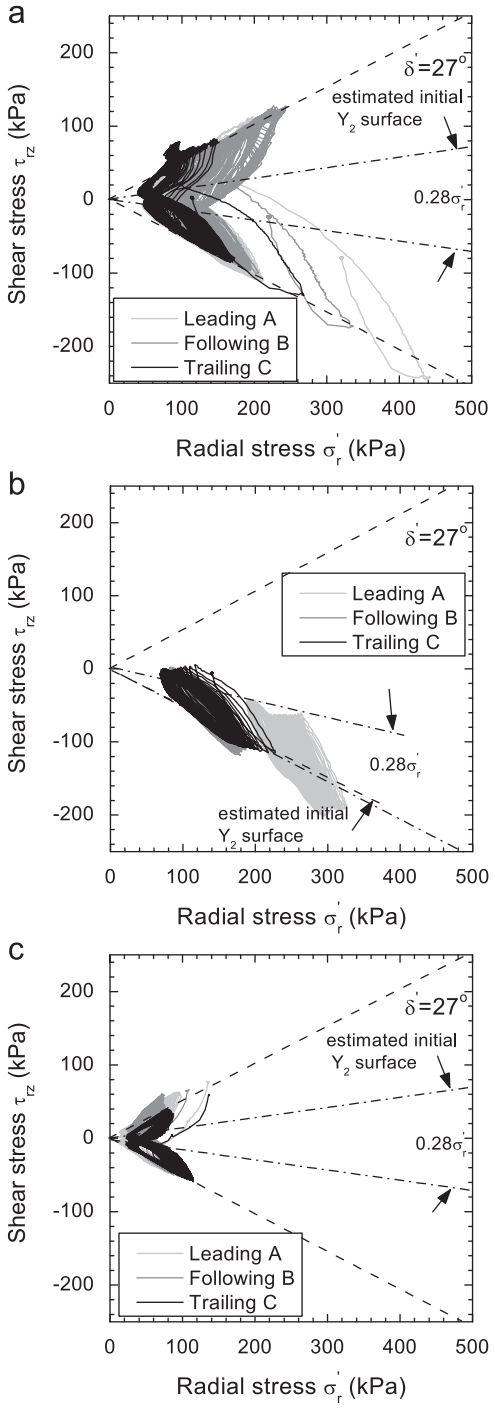


Fig. 22. Effective stress paths at all SSTs during example *Unstable* tests. (a) ICP2-TW1, (b) ICP3-OW1 and (c) ICP3-TW2.

4. Summary and conclusions

Model CC pile experiments on dry sand have shown similarly marked effects, from potentially severe capacity losses under slowly drained cyclic loading to full-scale piles driven to depths below the water table. Cyclic loading effects, which are often neglected in routine design, can strongly impact the foundation behaviour. The highly instrumented experiments described in the present paper offer new insights into the degradation processes by exploring the local effective stress conditions and relating them to the fundamental behaviour of sand. The main conclusions are as follows:

1. A simple scheme may be established among the normalised cyclic load amplitudes, the mean load levels and the number of cycles to failure that identifies conditions under which cyclic behaviour can be *Stable*, *Meta-Stable* or *Unstable*. At least 1000 cycles can be applied within the *Stable* Zone without degrading the capacity, while excursions into the other two regions are only likely to be acceptable in cases where the critical cyclic loading events are sufficiently infrequent for the negative effects on capacity to be sustained.
2. Under *Stable* loading conditions, up to 1000 cycles can be applied without the development of any interface local slip, over most of the shaft length and with most soil elements remaining within their initial Y_2 yield surfaces. The behaviour may be locally inelastic at the interface, but there is no large scale tendency for radial contraction to develop. Minor top-down shaft degradation may take place, but its progression is balanced and overcome by capacity growth through local densification and fabric rearrangement. Overall, the shaft capacity increases.
3. *Unstable* loading conditions invoke markedly inelastic behaviour both (i) in the soil mass, which tends to densify and lose mean stress, and (ii) at the interface where local slip develops due to shear zone compaction and marked σ_r' reductions. Shaft failure occurs in less than 100 cycles, governed by the Coulomb law that applies in interface ring shear tests. Hysteretic "butterfly-wing" effective stress paths develop close to the pile shaft and local failure progresses from the pile top downwards. Displacements may accelerate towards failure, or reverse in two-way tests when shaft capacity reductions make tension loading more critical than compression. Shaft capacities degrade markedly.
4. *Meta-Stable* loading leads to a response between these limits. Interface slip, hysteretic stress paths, mean stress state migration and shaft capacity reductions may all develop, depending on the cyclic loading levels imposed. However, piles can sustain hundreds of *Meta-Stable* cycles without failing, and markedly plastic (post-Y_2) behaviour is concentrated close to the shaft.

Procedures, such as those outlined by Jardine et al. (2005) that predict the radial effective stress and shaft

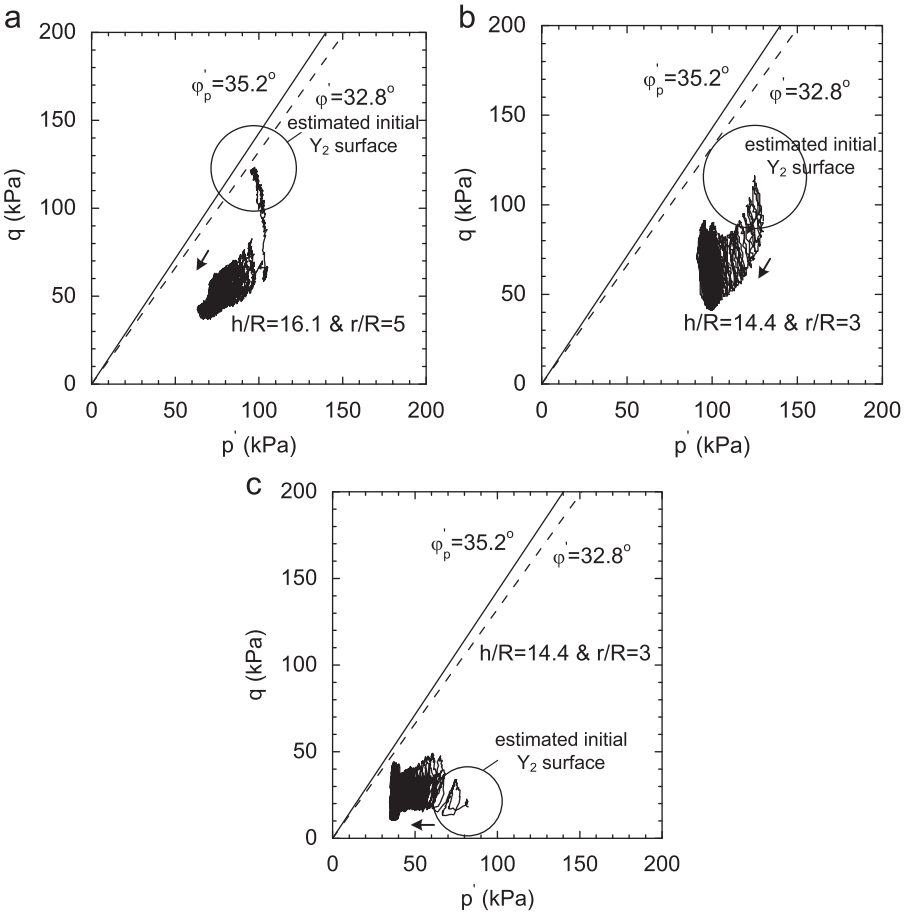


Fig. 23. Effective stress paths developed in sand mass at $5R$, $h/R \approx 15$ during example Unstable tests. (a) ICP2-TW1, (b) ICP3-OW1 and (c) ICP3-TW2.

capacity changes experienced under cyclic loading, are now being used in practical design. The experiments described above offer (i) mechanical explanations for the processes involved and (ii) a data set against which alternative theoretical-, numerical- or laboratory-based approaches may be evaluated and calibrated.

Acknowledgements

The authors gratefully acknowledge the support of Shell U.K., the UK Health and Safety Executive, the UK Engineering Physical Sciences Research Council, Total France, Centre National de la Recherche Scientifique (CNRS), the French Programme ANR SOLCYP, UK Royal Society and the Natural Science Foundation of China (Nos. 51011130162 and 51178421). The authors also extend their thanks to Mr. S. Ackerley, Mr. A. Bolsher, Mr. C. Dalton, Dr. M. Emerson, Mr. F. La Malfa, Mr. M. B. Rey and Mr. M. J.B. Toni for their contributions.

References

API American Petroleum Institute, 2008. Recommended Practice for Planning, Designing and Constructing Fixed Offshore Platforms—RP 2A-WSD.

Airey, D.W., Al-Douri, R.H., Poulos, H.G., 1992. Estimation of pile friction degradation from shearbox tests. Geotechnical Testing Journal 15 (4), 388–392.

Al-Douri, R., Poulos, H.G., 1994. Cyclic behaviour of pile groups in calcareous sediments. Soils and Foundations 34 (2), 49–59.

Altuhafi, F., Jardine, R.J., 2011. Effect of particle breakage and strain path reversal on the properties of sands located near to driven piles. In: Chung et al. (Eds.), Proceedings of Deformation Characteristics of Geomaterials, vol. 1. IS-Seoul, Pub., Hanrimwon, Seoul. pp. 386–395.

Bolton, M.D., Gui, M.W., Garnier, J., Corte, J.F., Bagge, G., Laue, J., Renzi, R., 1999. Centrifuge cone penetration tests in sand. Géotechnique 49 (4), 543–552.

Bowman, E.T., Soga, K., 2005. Mechanisms of set-up of displacement piles in sand: laboratory creep tests. Canadian Geotechnical Journal 42 (5), 1391–1407.

Chan, S., Hanna, T.H., 1980. Repeated loading on single piles in sand. Journal of the Geotechnical Engineering Division, American Society of Civil Engineers 106 (2), 171–188.

Chow, F.C., 1997. Investigations into Displacement Pile Behaviour for Offshore Foundations. Ph.D. Thesis. Imperial College, University of London.

Chow, F.C., Jardine, R.J., Brucy, F., Nauroy, J.F., 1998. The effects of time on the capacity of pipe piles in dense marine sand. American Society of Civil Engineers, Journal of Geotechnical and Geoenvironmental Engineering 124 (3), 254–264.

D'Aguiar, S.C., Caballero, F.L., Razavi, A.M.F., 2009. Piles under cyclic loading: study of the friction fatigue and its importance in piles behaviour. In: Proceedings of the 17th International Conference on Soil Mechanics and Geotechnical Engineering, vol. 2. Alexandria, Egypt, pp. 1313–1316.

DeJong, J.T., Randolph, M.F., White, D.J., 2003. Interface load transfer degradation during cyclic loading: a microscale investigation. Soils and Foundations 43 (4), 91–94.

DeJong, J.T., White, D.J., Randolph, M.F., 2006. Microscale observation and modelling of soil–structure interface behaviour using PIV. Soils and Foundations 46 (1), 15–28.

Fakharian, K., Evgin, E., 1997. Cyclic simple-shear behaviour of sand–steel interfaces under constant normal stiffness condition. Journal of Geotechnical and Geoenvironmental Engineering, American Society of Civil Engineers 123 (12), 1096–1105.

Ishihara, K., Tatsuoka, F., Yasua, S., 1975. Undrained deformation and liquefaction of sand under cyclic stresses. Soils and Foundations 15 (1), 29–44.

Jardine, R.J., 1991. The cyclic behaviour of offshore piles. In: O'Reilly, M.P., Brown, S.F. (Eds.), The Cyclic Loading of Soils. Blackie and Son, Glasgow.

Jardine, R.J., 1992. Some observations on the kinematic nature of soil stiffness. Soils and Foundations 32 (2), 111–124.

Jardine, R.J., 1994. Offshore Pile Design for Cyclic Loading: North Sea Clays. HSE Offshore Technology Report, OTN 94 157.85.

Jardine, R.J., Standing, R.J., 2000. Pile Load Testing Performed for HSE Cyclic Loading Study at Dunkirk, France. Two Volumes. Offshore Technology Report OTO2000 007. Health and Safety Executive, London, 60 p and 200 p.

Jardine, R.J., Chow, F.C., Overy, R., Standing, J.R., 2005. ICP Design Methods for Driven Piles in Sands and Clays. Thomas Telford, London, UK.

Jardine, R.J., Standing, J.R., Chow, F.C., 2006. Some observations of the effects of time on the capacity of piles driven in sand. Géotechnique 56 (4), 227–244.

Jardine, R.J., Zhu, B.T., Foray, P., Dalton, C.P., 2009. Experimental arrangements for the investigation of soil stresses developed around a displacement pile. Soils and Foundations 49 (5), 661–673.

Jardine, R.J., Zhu, B.T., Foray, P., Yang, Z.X. Measurement of stress field developed around closed-ended displacement piles in sand. Géotechnique, in press.

Jardine, R.J., Zhu, B.T., Foray, P., Yang, Z.X. Interpretation of stress measurements around closed-ended displacement piles in sand. Géotechnique, under review.

Kuwano, R., 1999. The Stiffness and Yielding Anisotropy of Sand. Ph.D. Thesis. Imperial College, University of London.

Kuwano, R., Jardine, R.J., 2007. A triaxial investigation of kinematic yielding in sand. Géotechnique 57 (7), 563–579.

Lehane, B.M., 1992. Experimental Investigations of Pile Behaviour Using Instrumented Field Piles. Ph.D. Thesis. Imperial College, University of London.

Lehane, B.M., Jardine, R.J., Bond, A.J., Frank, R., 1993. Mechanisms of shaft friction in sand from instrumented pile tests. Journal of Geotechnical and Geoenvironmental Engineering, American Society of Civil Engineers 119 (1), 19–35.

Le Kouby, A., Canou, J., Dupla, C., 2004. Behaviour of model piles subjected to cyclic axial loading. Cyclic Behaviour of Soils and Liquefaction Phenomena, 159–166 (Triantafyllidis (Ed.)).

Mortara, G., Mangiola, A., Ghionna, V.N., 2007. Cyclic shear stress degradation and post-cyclic behaviour from sand–steel interface direct shear tests. Canadian Geotechnical Journal 44 (7), 739–752.

Mortara, G., Ferrara, D., Fotia, G., 2010. Simple model for the cyclic behaviour of smooth sand–steel interfaces. Journal of Geotechnical and Geoenvironmental Engineering, American Society of Civil Engineers 136 (7), 1004–1009.

Poulos, H.G., 1989. Cyclic axial loading analysis of piles in sand. Journal of Geotechnical and Geoenvironmental Engineering 115 (6), 836–851.

Rimoy, S.P., Jardine, R.J., 2011. Strain accumulation in a silica sand due to creep after normal compression, and during sustained low-level cyclic loading. In: Chung et al. (Eds.), Proceedings of the Deformation Characteristics of Geomaterials, vol. 1. IS-Seoul, Pub., Hanrimwon, Seoul, pp. 463–470.

Salgado, R., Mitchell, J.K., Jamiolkowski, M., 1998. Calibration chamber size effects on penetration resistance in sand. Journal of Geotechnical and Geoenvironmental Engineering, American Society of Civil Engineers 124 (9), 878–888.

Tabucanon, J.T., Airey, D.W., Poulos, H.G., 1995. Pile skin friction in sands from constant normal stiffness tests. Geotechnical Testing Journal 18 (3), 350–364.

Tatsuoka, F., Jardine, R.J., Lo Presti, D., Di Benedetto, H., Kodaka, T., 1997. Characterising the pre-failure deformation properties of geomaterials: theme lecture for plenary session no. 1. In: Proceedings of the 14th International Conference on Soil Mechanics and Geotechnical Engineering, vol. 4. Hamburg, pp. 2129–2164.

Vucetic, M., 1994. Cyclic threshold shear strains in soils. Journal of Geotechnical Engineering, American Society of Civil Engineers 120 (12), 2208–2228.

White., D.J., Bolton, M.D., 2004. Displacement and strain paths during plane-strain model pile installation in sand. Géotechnique 54 (6), 375–397.

White, D.J., Zhao, Y., 2006. A model-scale investigation into 'set-up' of displacement piles in sand. In: Proceedings of the Sixth International Conference on Physical Modelling in Geotechnics—6th ICPMG '06, pp. 889–894.

Yang, Z.X., Jardine, R.J., Zhu, B.T., Foray, P., Tsuha, C.H.C., 2010. Sand grain crushing and interface shearing during displacement pile installation in sand. Géotechnique 60 (6), 469–482.

Zhu, B.T., Jardine, R.J., Foray, P., 2009. The use of miniature soil stress measuring sensors in applications involving stress reversals. Soils and Foundations 49 (5), 675–688.